The Effect of Sub-micron Second-phase Particles on the Rate of Grain Refinement in Copper during Cold Spray

Yinyin Zhang[1], Nicolas Brodusch[1], Sylvie Descartes[2], J. Michael Shockley[1^], Raynald Gauvin[1], Richard R. Chromik[1*]

[1]Department of Mining and Materials Engineering, McGill University, 3610 University Street, Montreal, QC, Canada, H3A 0C5
[2]Université de Lyon, CNRS, INSA-Lyon, LaMCoS, UMR5259, F-69621 Villeurbanne, France
[^]Current affiliation: NRC Postdoctoral Research Associate, sited in Chemistry Division, US Naval Research Lab, Washington, DC
*Corresponding author: richard.chromik@mcgill.ca

Abstract

The effect of non-deformable submicron second-phase particles (d = 200-500 nm) on microstructural refinement during cold spray was examined. Using single particle impact testing, two types of splats were fabricated using two different feedstocks: a Cu-0.21wt.%O powder containing Cu_2O second-phase particles and a single-phase Cu. Microstructural evolution analysis using high-resolution electron backscatter diffraction (EBSD) shows grain refinement occurred at a higher rate in the Cu-0.21wt.%O powder. That was due to dynamic recrystallization initiated by particle stimulated nucleation (PSN). High strain rate deformation of cold spray was found to be the key to activate PSN. The present study suggests cold spray is a possible technique to fabricate ultra-fine grained materials by using feedstock containing second-phase particles.

Key words: Cold spray; second-phase particles; high-resolution electron backscatter diffraction (EBSD); particle stimulated nucleation (PSN).

1.   Introduction

For cold sprayed metals, one often finds fully recrystallized microstructures with grain sizes in the range of tens to hundreds of nanometers. In some instances, these microstructures are constrained to particle boundaries, which experience the highest strains and strain rates compared to the center of the particles. However, in some instances, such as spraying of CP-Ti using helium, one observes that the entire coating exhibits a fine-grained recrystallized microstructure (Ref 1, 2). Ultrafine-grained microstructure exhibits improved mechanical properties such as enhanced strength and good ductility (Ref 3). In fact, bulk versions of such microstructure are routinely fabricated by severe plastic deformation (SPD) processes (ε up to 10) such as equal channel angular extrusion (ECAE) (Ref 4, 5) and dynamic plastic deformation (DPD) (Ref 6).

The ability of cold spray to provide a homogeneous, fully recrystallized microstructure strongly depends on the consistency and quality of the powders used in the process. Powders manufacturers often list ranges of possible oxygen content in their powders, with those most pure, i.e. with the least oxygen, being the most expensive. Oxygen can be detrimental in a number of ways, but within the scope of microstructural evolution under high strains and strain rates, the presence of second-phase metal-oxide inclusions can have a profound effect. It is well known that the presence of non-deformable second-phase particles can either retard or accelerate the rate of grain refinement, i.e. dynamic recrystallization, during SPD process, and that largely depends on size of the second-phase particles. Nano-scale particles (d < 100 nm) are found to decrease the grain refinement rate because they inhibit recovery and grain boundary migration (Ref 4). Nevertheless, large micron-scale second-phase (d >1 µm) effectively increase grain refinement rate as they facilitate development of new high angle grain boundaries in the surrounding matrix and thus provide sites for particle stimulated nucleation (PSN) (Ref 5). The above mechanisms of the influence of hard second-phase particles on grain refinement rate are also observed in static recrystallization at conventional strains (ε up to 0.5) (Ref 7-10).

In this paper, the potential of cold spray for manufacturing ultrafine-grained materials was examined by investigation of microstructural evolution and deformation mechanisms of a two-phase Cu-O powder and a single-phase Cu powder. In order to eliminate microstructural changes because of heating that could be induced by multiple particle impacts and extended exposure to the heated high pressure gas, a single particle impact test was performed aiming to obtain individual splats.

2.   Experimental and materials

A gas atomized Cu-0.21wt.%O powder (Tekna Advanced Materials Inc., Canada) with mean size of 17.4 µm in diameter was used as feedstock, as seen in Fig. 1a. In Fig. 1b, a cross section of the powder shows size (200-500 nm diameter) and distribution of the second-phase particles within the Cu matrix. Energy dispersive X-ray spectroscopy (EDX) spectra indicates the higher oxygen content of the second-phase particles (see Fig. 1c) and Raman spectroscopy identified them as Cu_2O (Ref 11), evidenced by its characteristic peaks at around 200 cm^{-1} and 650 cm^{-1} (see Fig. 1d). The particle volume fraction measured by pixel counting software (Image J) was approximately 5%. In order to observe influence of the second-phase particles on microstructural evolution during impact, a single-phase Cu with low oxygen content of 0.06 wt.%O was used as a reference and was cold sprayed under identical conditions.
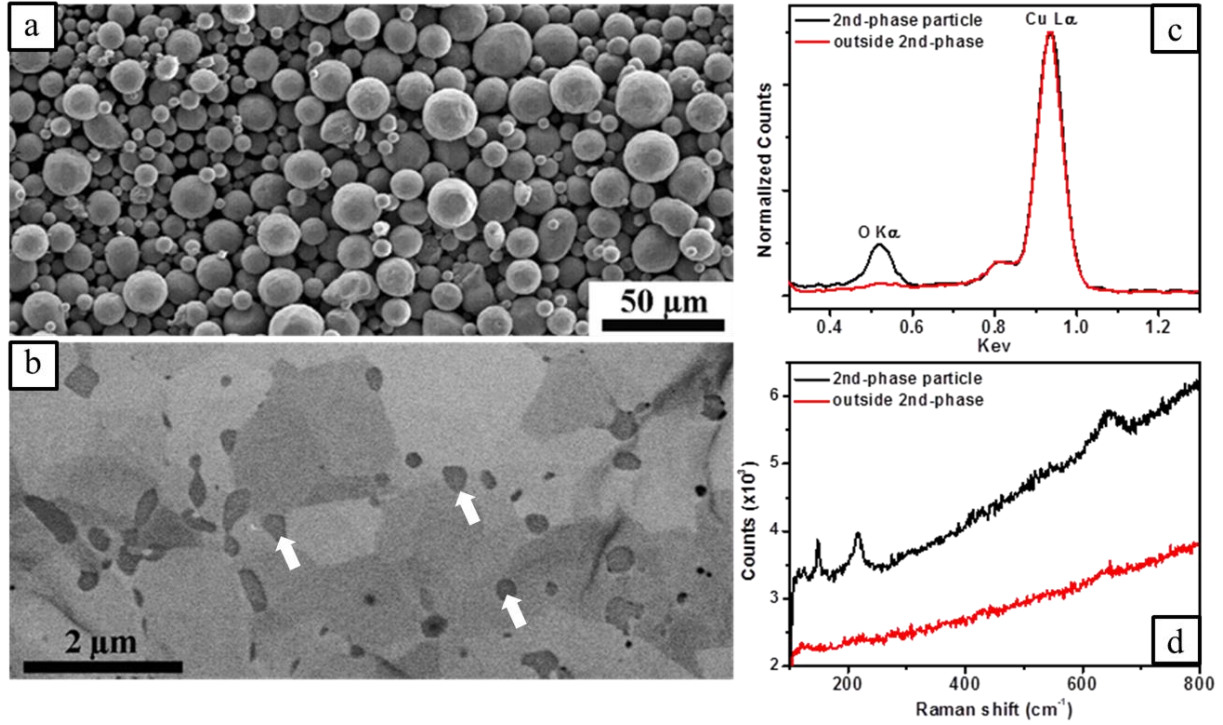
Figure 1. (a) secondary electron image of the powder; (b) backscattered electron image of the cross section of the as-received Cu-0.21wt% O powder, where white arrows indicate some of the second-phase particles; (c) EDX and (d) Raman spectroscopy analysis of the second-phase particles and areas outside the second-phase particles.

The single particle impact tests were conducted by a commercially available cold spray system (PCS800, Plasma Giken, Japan) using a low feed rate of 0.1 g/min and a high gun traverse speed of 1000 mm/s. Nitrogen was used as the process gas and the gas pressure and preheat temperature were maintained at 5 MPa and 800°C, respectively. CP-Ti (McMaster Carr) ($HV_{0.2}$ = 170) was used as substrate. The microstructure of as-sprayed splats were characterized by high resolution electron backscatter diffraction (EBSD). Cross-sections of the splats were mounted, mechanically ground and polished, followed by vibratory polishing using colloidal silica for 3 hours. To reduce the high charging build-up at the splat/resin interface, a solution of 1-butyl-3-methylimidazolium tetrafluoroborate ($BMI-BF_4$) ionic liquid in ethanol (Ref 12, 13) was spilled in the gap between the resin and finally Ar^+ ion beam milling for 0.5 hours. EBSD orientation maps were acquired with an accelerating voltage of 15 kV with a SU-8000 cold field-emission SEM (Hitachi High-Technologies, Japan) equipped with the automated HKL Channel5 Flamenco software. HKL Channel5 Tango was used for EBSD data analysis, where high angle grain boundaries (HAGBs) were defined as being greater or equal to 15° in misorientation and those with misorientation less than 15° defined as low angle grain boundaries (LAGBs). To eliminate excessive misorientation noise, boundaries of less than 2° were cut off and a factor of 5 was used when performing noise reduction using HKL Channel5 Flamenco software. Note that the Ti substrate and the second-phase Cu_2O particles were not considered for indexing.

3.   Results and discussion

Fig. 2a and 2b show backscattered electron (BSE) micrographs of the cross sections of the as-sprayed splats without and with the second-phase particles, namely single-phase and two-phase splats, respectively. The flattening ratio (R) of the splat, length divided by height serves as a measure of the degree of deformation of the splats, with $R_{single-phase}$ =3.35 being much higher than $R_{two-phse}$ = 2.33. That suggests more severe deformation occurred in the single-phase splat at identical spraying conditions. Corresponding orientation EBSD maps are shown in Fig. 2c and 2d, where both splats exhibit overall inhomogeneous microstructure containing coarse grains generally in the upper part of the splats and fine grains close to the interface of splats and substrates. However, the splats show distinct differences in microstructural refinement. The two-phase splat has a larger refined zone than the single-phase splat. Statistical measurements of grain sizes in the two splats show the area fraction of sub-micron size grains (<1 µm) was much higher in the two-phase splat (38%) than that in the single-phase splat (12%).
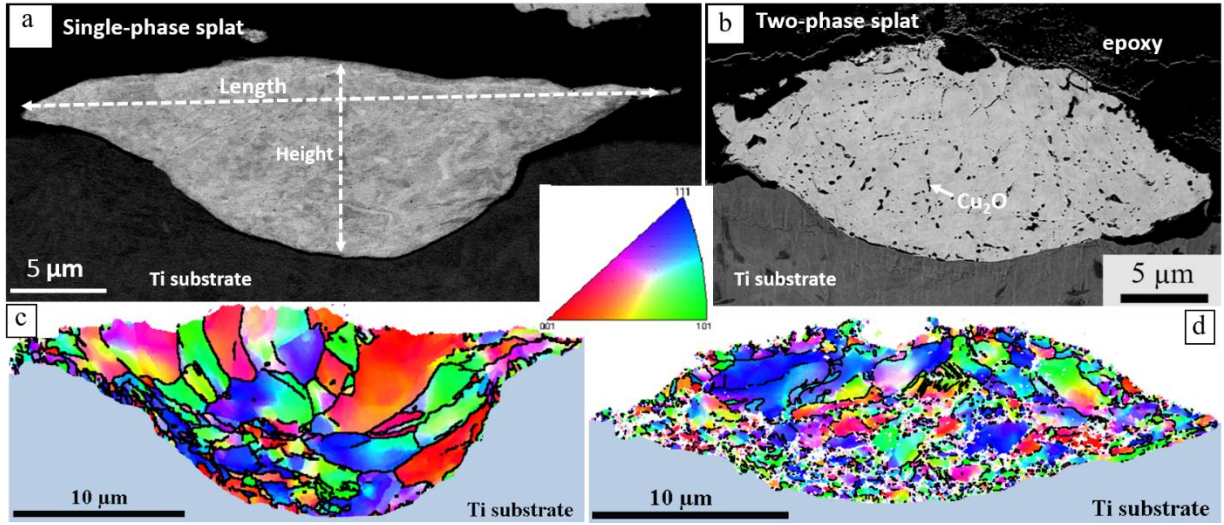
Figure 2. BSE micrographs of cross sections of the as-sprayed (a) single-phase splat, where length and height of the splats were denoted as dashed lines; (b) two-phase splat, in which dark contrast inside the splat was Cu_2O particles; Corresponding EBSD maps are shown in (c) single-phase splat and (d) two-phase splat. For the EBSD maps, Ti substrate beneath the splats were not indexed and therefore was filled with uniform light blue for visual simplicity. Above the splats was the mounting epoxy with and ionic liquid (BMI-BF_4) filling the gap between the epoxy and the splat. Only high angle grain boundaries (>15°) were presented as black lines.

3.1 Microstructural evolution of the single-phase splat

Fig. 3 is an EBSD map corresponding to the rectangle marked in the inset. During impact, the powder boundary experienced shear deformation which is along the interface of the splat and the substrate. Following the arrow **a**, which is perpendicular to the shear direction, 4 different zones can be found according to their deformation, as marked in Fig. 3. The point-to-point and the point-to-origin misorientation along arrows **a-e** are plotted versus distance in Fig. 4 a-e, respectively. The arrow **a** represents microstructural evolution from the splat center to the edge,

4

while **b-e** are along the shear direction in zones 1-4. They exhibit distinct microstructure, grain boundary misorientation, and misorientation gradient in different zones.

In the splat center (zone 1), where the least deformation was expected (Ref 14), LAGBs are randomly distributed in the initial large grains. A few subgrain boundaries are formed based on the point-to-point misorientation measurement (Fig. 4b). The misorientation gradient in this zone is relatively low (point-to-origin misorientation in Fig. 4b), suggesting relatively low lattice strain and dislocation density.

Approaching the splat interface, in zone 2, some grains are divided by well-defined subgrains that are along shear direction (arrow **c**), forming elongated grains with an average transverse spacing of approximately 400 nm. Except for those subgrains, the misorientation gradient in both directions are still relatively low (point-to-origin misorientation in Fig. 4a and 4c).

In zone 3, stress and strain increase and well-defined elongated grains are formed with a width of around 440 nm, similar to the average transverse LAGB spacing in zone 2, suggesting the newly formed HAGBs are through rotation of the LAGBs. This deformation mechanism in cold spray has been studied and well established (Ref 15, 16). The point-to-point misorientation along the shear direction (Fig. 4d) exhibits a large amount of formation of subgrain boundaries. In the splat/substrate interface (zone 4), there are some equiaxed grains in the sizes of around 300 nm. The point-to-point misorientation (Fig. 4e) shows very low grain boundaries inside the well-defined grains, meaning subgrains barely exist at this moment. The point-to-origin plot (Fig. 4e) shows almost no change in misorientation inside the grains. Therefore, the microstructure has fully recrystallized at the splat boundary.
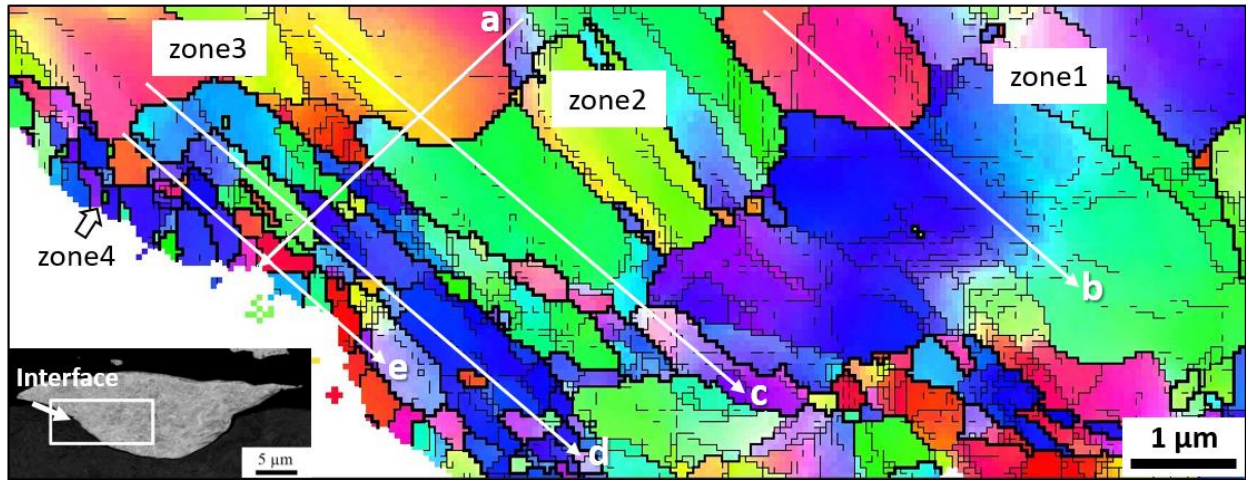
Figure 3. EBSD map of the single-phase splat in the rectangle marked in the inset. It reveals microstructure evolution with deformation, i.e. along the arrow **a**, and it can be identified as zone 1, 2, 3, and 4. Grain boundaries are plotted as three groups based on misorientation: <15°, 15°-30°, and >30°, shown as black lines with low, medium, and high thickness. Arrows **b-e** represent directions that are along shear deformation.
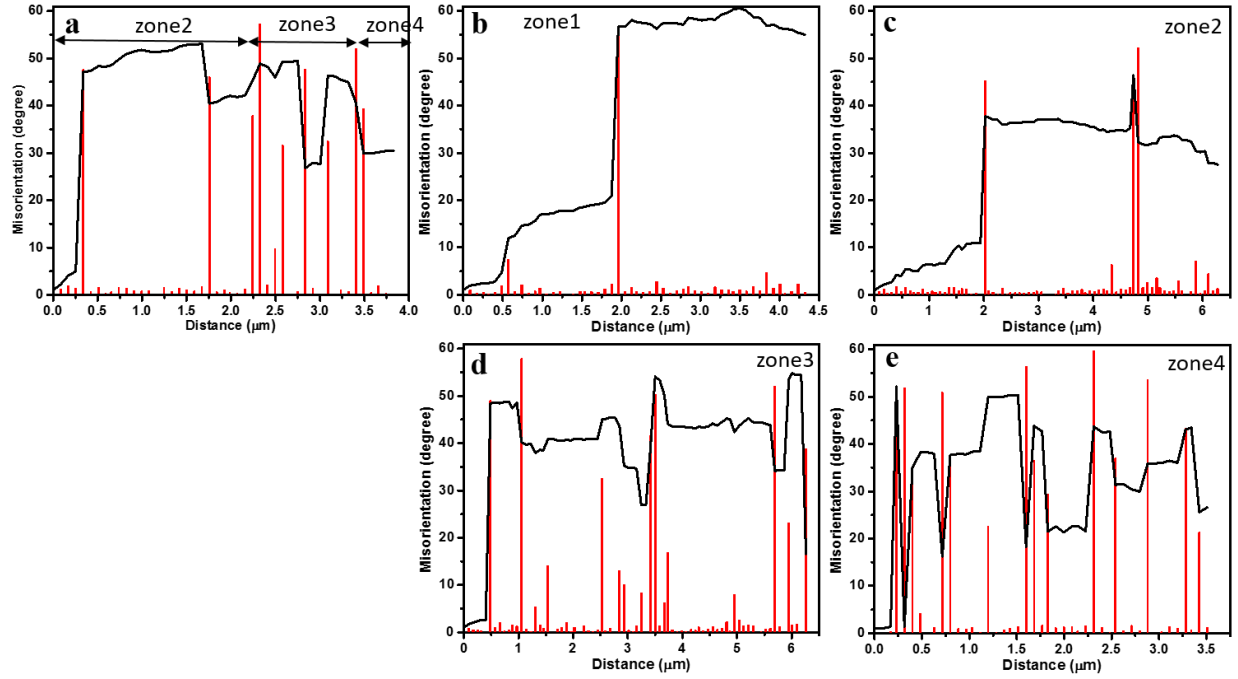
Figure 4. Misorientation profiles of the single-phase splat, showing point-to-point (the column charts) and point-to-origin (the line plots) along the arrows of **a**, **b**, **c**, **d**, and **e**, respectively that are marked in Fig. 3.

3.2 Microstructural evolution of the two-phase splat

Fig. 5 are EBSD maps of the splat center (zone 1) and splat boundary (zone 2) that are corresponding to the boxes highlighted in the insets, respectively. The point-to-point and the point-to-origin misorientation along the arrows **a-d** marked in Fig. 5 are plotted in Fig. 6. Again, the arrows **a** and **c** represent microstructural evolution perpendicular to the shear deformation, while arrows **b** and **d** show microstructure along the shear direction.

At the splat center (Fig. 5a), subgrain boundaries have been formed, suggesting relatively high lattice strain and dislocation density in this region. The misorientation gradients along both directions in this region (point-to-origin misorientation in Fig. 6a and 6b) are high and point-to-point misorientation charts show frequent presence of grain boundaries of around 10°, which can be served as subgrains. Close to the second-phase particles (see the thick white arrow in Fig. 5a), high angle grain boundaries (>45°) are formed. Previous study on AA8079 alloy during equal channel angular pressing (ECAP) reported similar results and they proposed a deformation mechanism (Ref 5). Deformation zones containing large local misorientation gradients were formed firstly in the vicinity of the second-phase particles and tended to link the closest particles. Further deformation was therefore confined in those zones and new HAGBs were conceived (Ref 5). Comparing to the center of the single-phase splat, a higher rate formation of LAGBs and HAGBs were observed, therefore the grain refinement has begun even at the splat center.

Towards interfacial region of the splat and the substrate (Fig. 5b), strain increases and grains are further refined, leading to equiaxed grains in a size of approximately 360 nm, the same order of magnitude as that in the single-phase splat boundary (around 300 nm). This implies a stable state might be reached, which is consistent with Apps et al.'s result, where similar structure was

obtained in a particle-containing AA8079 aluminum alloy and its single-phase counterpart when approaching very high strain (ε up to 10) (Ref 5). However, for the two-phase splat, most of the grains in zone 2 contain subgrains and LAGBs (Fig. 5b). Point-to-point misorientation along both directions (Fig. 6c and 6d) reveal grain boundaries of around 10-15°, which makes it different from that in the zone 4 of the single-phase splat (Fig. 3), where the material has experienced fully recrystallization and no such LAGBs are further developed.
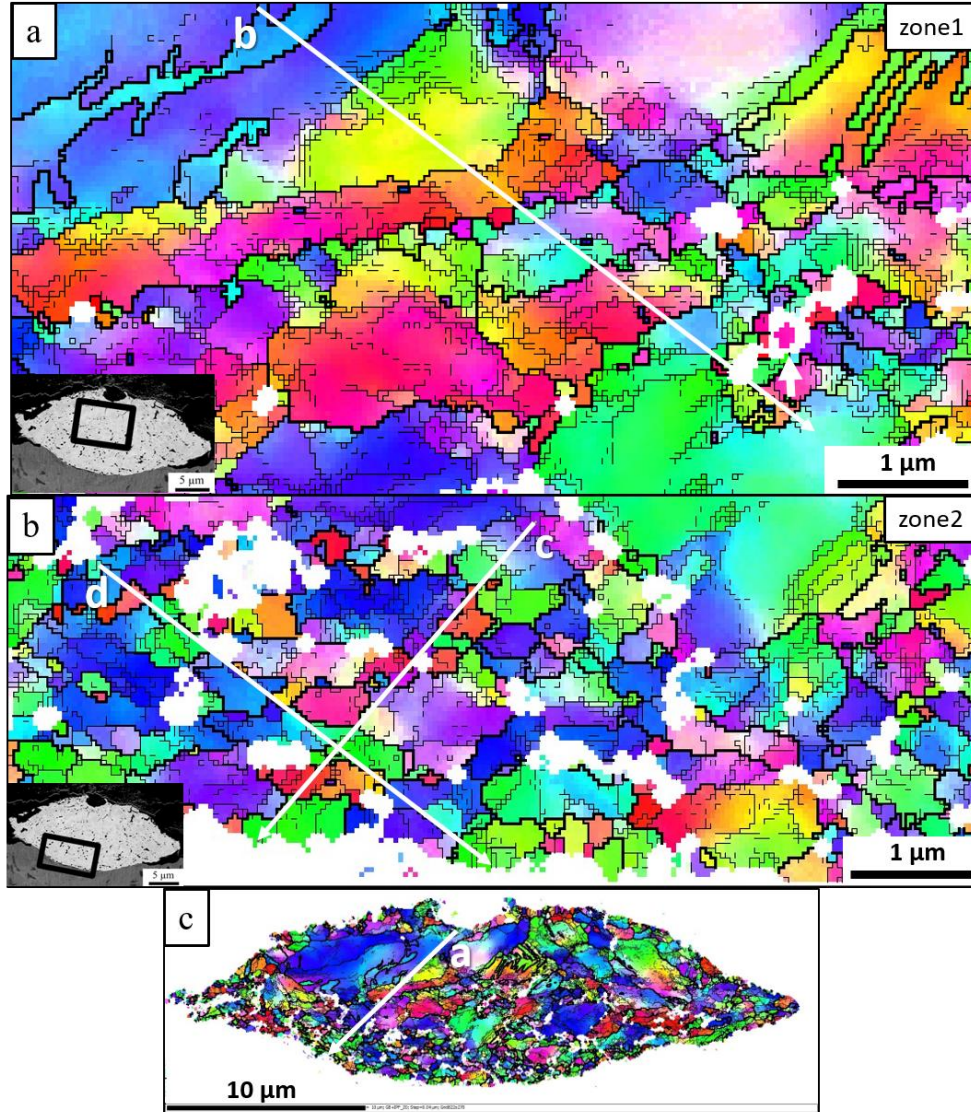
Figure 5. (a) EBSD map of the center of the two-phase splat, shown as a rectangle in the inset. The thick white arrow indicates second-phase particles, which were not indexed. (b) shows EBSD map of the splat boundary, marked as a rectangle in the inset. (c) EBSD map of the whole splat. Grain boundaries are plotted as three groups: <15°, 15°-30°, and >30°, shown as black lines with low, medium, and high thickness. The white color inside the splat are second-phase particles that were not indexed, while outside the splat are either Ti substrate or epoxy which were not indexed. Long white arrows of **a, b, c** and **d** indicate directions of misorientation profiles in Fig. 6.

7
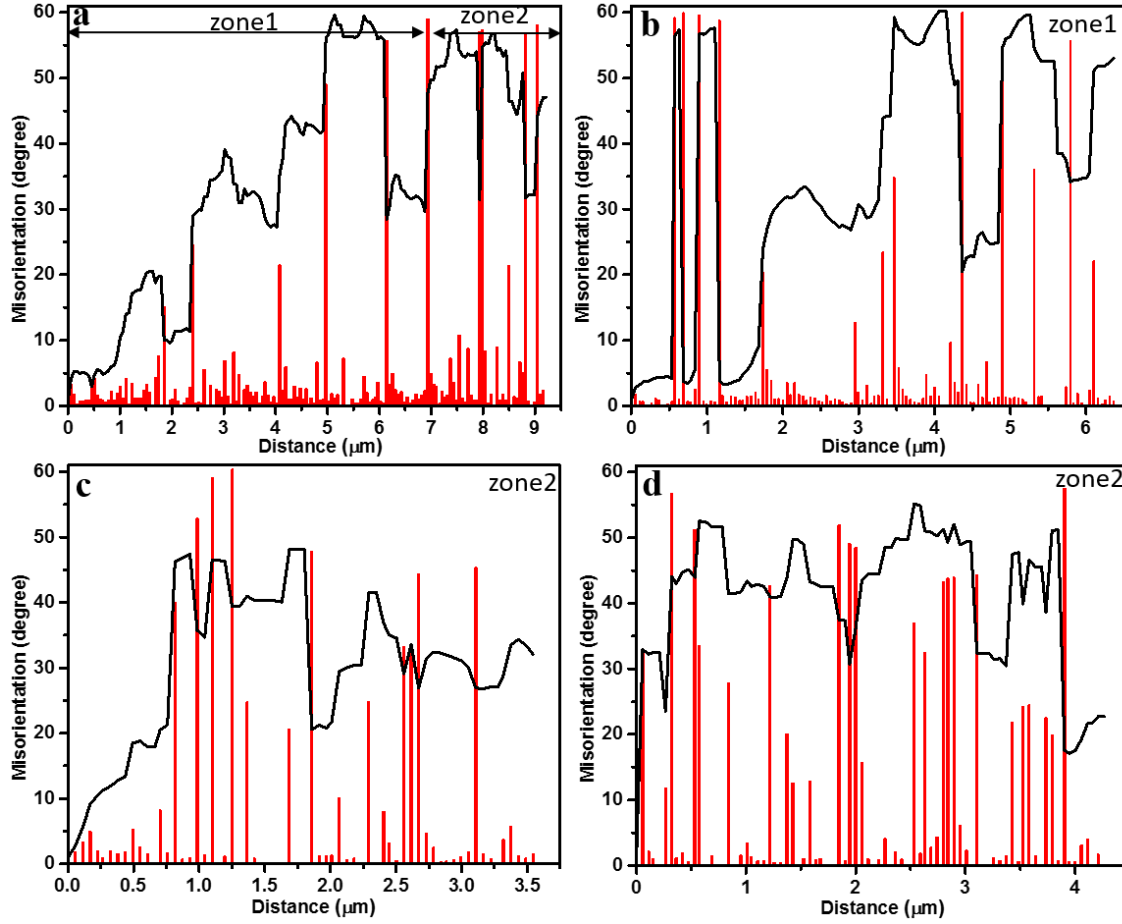
Figure 6. Misorientation profiles of the two-phase splat, showing point-to-point (the column charts) and point-to-origin (the line plots) along the arrows of **a, b, c** and **d,** respectively that are marked in Fig. 5.

3.3 Influence of the second-phase particles on deformation mechanism during cold spray

Micron-scale second-phase particles are well known to increase grain refinement rate during both dynamic and static recrystallization comparing to their single-phase counterparts (Ref 5, 17). However, in this study, submicron second-phase particles are found to behave the same way. That could be due to the influence of high strain rate introduced by supersonic velocity impact during cold spray. Finite element simulation shows for a 10 µm Cu powder with speed of 900 ms^{-1} (824 ± 63 ms^{-1} in the present study) strain rate distribution ranges between 0.2×10^8 and 0.6×10^9 s^{-1} from the splat center to the boundary right after impact (Ref 14). On the other hand, material response at high strain rates such as that of pure Cu has been studied extensively. For strain rates higher than 10^3 s^{-1}, dislocation accumulation rate increased dramatically (Ref 18). Even at low strains, e.g. $\varepsilon = 0.05$, Cu contains dislocation density of $\rho \sim 5 \times 10^{13}$ m^{-2} (Ref 18). At high strains ($\varepsilon > 1$), however, dynamic recrystallization takes place because adiabatic temperature rise induced by high strain rates is significant (Ref 15, 19). For example, it was calculated the temperatures can reach 500-800 K in shock-loaded pure Cu at high strain ($\varepsilon \sim 3$-4) and strain rate ($\dot{\varepsilon} \sim 10^4$ s^{-1}), and that temperature is consistent with its onset of static recrystallization temperature of 523 K (Ref 19). Therefore, by high strain-rates, the propensity of dynamic recrystallization is enhanced due to rapid dislocation generation and/or adiabatic heating. High

dislocation densities have been widely observed in cold sprayed Cu by TEM and ECCI techniques (Ref 20, 21). It was also found that a large number of dislocation loops were generated during or immediately after deformation and that is most likely due to the agglomeration of point defects induced by dislocation climb (Ref 22). At the splat boundary, where the material undergoes high strain and strain rate, the ultrafine grains were interpreted as dynamic recrystallized microstructure in FCC metals (Ref 16, 21), which is consistent with the present observation.

Whether the presence of second-phase particles can provide sites of recrystallization nucleation largely depends on dislocation structures around them (Ref 23). In particle deformation zones, complex dislocation structures associated with local lattice rotations should be formed to initiate particle stimulated nucleation of recrystallization (PSN), while the generation of prismatic loops only, which is called laminar motion, is not able to activate PSN due to their low energy (Ref 23). Using a dislocation plasticity model, proposed by Brown (Ref 24), the transition from laminar to rotational motion at a particle diameter d may occur at a dislocation density (ρ) given by:

$$\rho = \frac{b^2}{d^4} \left(\frac{\sqrt{2}\alpha\mu}{\sigma_f}\right)^2$$
(eq.1)

Where b is the Burgers vector, α a constant of ~0.5, μ the shear modulus, σ_f the friction stress in the matrix. When typical values of Cu for all the constants (b = 0.26 nm, μ = 4.2×10^{10} Nm^{-2} (Ref 23), σ_f = 4.2×10^6 Nm^{-2} (Ref 24)) are inserted, a critical dislocation density for a submicron particle, e.g. 500 nm, is around 5.4 ×10^{13} m^{-2}, which can be easily obtained at high strain rate deformation even at low strains, e.g. ε = 0.05. This suggests PSN can be activated around submicron second-phase particles during high strain rate deformation. Therefore, deformation zones containing large local misorientation gradients were formed, as well as new high angle grain boundaries around the second-phase particles (Fig. 5a). Towards the splat boundary (Fig. 5b), where strain and strain rate were high, dynamic recrystallization based on PSN was well developed, leading to a homogeneous microstructure of ultrafine grains.

Therefore, oxygen as second-phase inclusions in the feedstock helped to produce ultrafine-grained microstructure using cold spray, unlike the single-phase counterpart where only a small fraction of fine grains was constrained in the splat boundary. With better control of process parameters, it is possible to utilize feedstock containing second-phase particles to engineer microstructures with greater levels of recrystallization and ultrafine grains.

4.   Conclusions

In summary, the influence of the submicron second-phase particles (200-500 nm) on microstructural evolution and deformation mechanism of a two-phase Cu-O feedstock during cold spray was studied using EBSD technique. The rate of grain refinement was significantly increased in the two-phase splat even though it experienced lower strain level. Dynamic recrystallization by PSN was found to be the main microstructural refinement mechanism. Initiation of PSN by the current second-phase particle size was most likely due to the influence of ultra-high strain-rate deformation during cold spray, where rapid dislocation generation and adiabatic temperature rise occurred. The above results make cold spray a potential technique to fabricate ultra-fine grained microstructure by using feedstock containing second-phase particles.

Acknowledgements

References

1. D. Goldbaum, "Micromechanical testing of cold sprayed Ti splats and coatings," PhD Thesis, McGill University, 2012
2. P. Vo, D. Goldbaum, W. Wong, E. Irissou, J.-G. Legoux, R.R. Chromik, and S. Yue, Cold-spray processing of titanium and titanium alloys, *Titanium Powder Metallurgy: Science, Technology and Applications*, F.H.F. Ma Qian Ed., Elsevier, 2015, p. 405
3. R.Z. Valiev, Structure and mechanical properties of ultrafine-grained metals, *Materials Science and Engineering: A*, 1997, **234–236**, p. 59-66
4. P.J. Apps, M. Berta, and P.B. Prangnell, The effect of dispersoids on the grain refinement mechanisms during deformation of aluminium alloys to ultra-high strains, *Acta Materialia*, 2005, **53**(2), p. 499-511
5. P.J. Apps, J.R. Bowen, and P.B. Prangnell, The effect of coarse second-phase particles on the rate of grain refinement during severe deformation processing, *Acta Materialia*, 2003, **51**(10), p. 2811-2822
6. Y.S. Li, N.R. Tao, and K. Lu, Microstructural evolution and nanostructure formation in copper during dynamic plastic deformation at cryogenic temperatures, *Acta Materialia*, 2008, **56**(2), p. 230-241
7. M. Cahoreau, and F.J. Humphreys, The rotation of particles during the deformation of a two-phase copper alloy, *Acta Metallurgica*, 1984, **32**(9), p. 1365-1370
8. F.J. Humphreys, Local lattice rotations at second phase particles in deformed metals, *Acta Metallurgica*, 1979, **27**(12), p. 1801-1814
9. F.J. Humphreys, and M.G. Ardakani, Grain boundary migration and Zener pinning in particle-containing copper crystals, *Acta Materialia*, 1996, **44**(7), p. 2717-2727
10. F.J. Humphreys, and P.N. Kalu, The plasticity of particle-containing polycrystals, *Acta Metallurgica et Materialia*, 1990, **38**(6), p. 917-930
11. J. Hesse, and A. Compaan, Resonance Raman studies of annealing in He-, Na-, Cd-implanted cuprous oxide, *Journal of Applied Physics*, 1979, **50**(1), p. 206-213
12. N. Brodusch, H. Demers, and R. Gauvin, Ionic Liquid Used for Charge Compensation for High-Resolution Imaging and Analysis in the FE-SEM, *Microscopy and Microanalysis*, 2014, **20**(S3), p. 38-39
13. N. Brodusch, K. Waters, H. Demers, and R. Gauvin, Ionic liquid-based observation technique for nonconductive materials in the scanning electron microscope: Application to the characterization of a rare earth ore, *Microscopy research and technique*, 2014, **77**(3), p. 225-235
14. H. Assadi, F. Gärtner, T. Stoltenhoff, and H. Kreye, Bonding mechanism in cold gas spraying, *Acta Materialia*, 2003, **51**(15), p. 4379-4394
15. M. Meyers, J. LaSalvia, V. Nesterenko, Y. Chen, B. Kad, and T. McNelley, Recrystallization and related phenomena, *Proc Rex*, T. McNelley Ed., 1997, p. 279-286.
16. Y. Zou, W. Qin, E. Irissou, J.-G. Legoux, S. Yue, and J.A. Szpunar, Dynamic recrystallization in the particle/particle interfacial region of cold-sprayed nickel coating: Electron backscatter diffraction characterization, *Scripta Materialia*, 2009, **61**(9), p. 899-902

17. M.H. Lewis, and J.W. Martin, Yielding and work-hardening in internally oxidised copper alloys, *Acta Metallurgica*, 1963, **11**(11), p. 1207-1214

18. P. Follansbee, and U. Kocks, A constitutive description of the deformation of copper based on the use of the mechanical threshold stress as an internal state variable, *Acta Metallurgica*, 1988, **36**(1), p. 81-93

19. U. Andrade, M.A. Meyers, K.S. Vecchio, and A.H. Chokshi, Dynamic recrystallization in high-strain, high-strain-rate plastic deformation of copper, *Acta Metallurgica et Materialia*, 1994, **42**(9), p. 3183-3195

20. C. Borchers, F. Gärtner, T. Stoltenhoff, and H. Kreye, Microstructural bonding features of cold sprayed face centered cubic metals, *Journal of Applied Physics*, 2004, **96**(8), p. 4288-4292

21. Y. Zhang, N. Brodusch, S. Descartes, R.R. Chromik, and R. Gauvin, Microstructure refinement of cold-sprayed copper investigated by electron channeling contrast imaging, *Microscopy and Microanalysis*, 2014, **20**(05), p. 1499-1506

22. C. Borchers, F. Gärtner, T. Stoltenhoff, and H. Kreye, Formation of persistent dislocation loops by ultra-high strain-rate deformation during cold spraying, *Acta Materialia*, 2005, **53**(10), p. 2991-3000

23. A. Rollett, F. Humphreys, G.S. Rohrer, and M. Hatherly, Recrystallization and related annealing phenomena, Elsevier, 2004.

24. L. Brown, Transition from laminar to rotational motion in plasticity, *Philosophical Transactions of the Royal Society of London A: Mathematical, Physical and Engineering Sciences*, 1997, **355**(1731), p. 1979-1990